First-principles insight in structure-property relationships of hexagonal Si and Ge polytypes

Martin Keller [1], Abderrezak Belabbes [1,2], Jürgen Furthmüller [1], Friedhelm Bechstedt [1], and Silvana Botti [1]

[1]*Institut für Festkörpertheorie und -optik, Friedrich-Schiller-Universität Jena, Max-Wien-Platz 1, 07743 Jena, Germany*
[2]*Department of Physics, Sultan Qaboos University, P.O. Box 36, 123 Muscat, Oman*

Hexagonal SiGe is a promising material for combining electronic and photonic technologies. In this paper, the energetic, structural, elastic, and electronic properties of the hexagonal polytypes ($2H$, $4H$, and $6H$) of silicon and germanium are thoroughly analyzed under equilibrium conditions. For this purpose, we apply state-of-the-art density functional theory. The phase diagram, obtained in the framework of a generalized Ising model, shows that the diamond structure is the most stable under ambient conditions, but hexagonal modifications are close to the phase boundary, especially for Si. Our band structure calculations using the modified-Becke-Johnson–local-density-approximation (MBJLDA) and Heyd-Scuseria-Ernzerhof (HSE06) exchange-correlation functionals predict significant changes in electronic states with hexagonality. While Si crystals are always semiconductors with indirect band gaps, the hexagonal Ge polytypes have direct band gaps. The branch-point energies of the Si polytypes appear in the fundamental gaps, while for the Ge crystals they are below the valence band maxima. Band alignment based on the branch-point energy leads to type-I heterocrystalline interfaces between Ge polytypes, where electrons and holes can be trapped in the layer with the higher hexagonality.

I. INTRODUCTION

The group-IV elements silicon (Si) and germanium (Ge) crystallize under ambient conditions in a cubic diamond structure. The bonding is characterized by sp^3 hybridization, and consequently, the nearest-neighbor atoms form regular tetrahedra. However, under higher pressure several Si and Ge polymorphs with different coordination have been reported [1–8]. In addition, using various deposition and growth techniques, Si and Ge polytypes that differ from the diamond structure have also been observed.

Polytypism is a one-dimensional type of polymorphism which occurs, e.g., when the geometry of structural layers is preserved but the number of layers in the layer-stacking sequence is altered. In this setting, hexagonal polytypes of the diamond structure can be formed by keeping the tetrahedral coordination while varying the stacking sequence along the cubic [111] (corresponding to the hexagonal [0001]) direction [9]. As can be observed in Fig. 1, the resulting polytypes only differ in the manner in which Si or Ge bilayers are oriented along the stacking axis, yielding either a *chair* or a *boat* conformation. One may equivalently speak about the stacking of *eclipsed* or *staggered* bilayers [10]. In Ramsdell notation [11] the stacking in the diamond structure is purely chairlike (eclipsed) and denoted with $3C$, since periodicity in the [111] direction is reached after three cubic (C) bilayers. The space group is O_h^7 ($Fd3m$). The pure stacking of boatlike (staggered) conformers leads to the hexagonal lonsdaleite $2H$ structure with space group D_{6h}^4 ($P6_3/mmc$) and two hexagonal (H) bilayers to reach periodicity in the [0001] direction. In addition, in Fig. 1, two other hexagonal polytypes, $4H$ and $6H$, with four or six bilayers and, hence, 8 or 12 atoms in their hexagonal unit cells, are displayed. The space group of pH polytypes ($p = 2, 4, 6$) is still D_{6h}^4 ($P6_3/mmc$). The ratio

of the number of staggered bilayers to the total number of such layers gives the percentage of hexagonality h with 0% for $3C$, 33% for $6H$, 50% for $4H$, and 100% for $2H$. More complex arrangements of eclipsed and staggered bilayers can lead also to rhombohedral (R) polytypes pR with space group $R3m$ (C_{3v}^5).

Lonsdaleite $2H$ is the most studied polytype of Si after diamond $3C$ and has been synthesized using a variety of methods [12–18]. Lonsdaleite silicon is present in core-shell nanowires [16,19–21], and $4H$-Si nanoplatelets have been recently reported [22]. The transformation of cubic Si into hexagonal polytypes is also observed for high-temperature indentation [23], plastic deformation [24,25], ion implantation [26], low-pressure chemical vapor deposition [27], pulsed laser beam annealing [28], and nanoribbon growth [29]. It is worthwhile mentioning that the rhombohedral polytype $9R$ has been observed in Si nanowires [19,30]. Ribbons of lonsdaleite Ge were produced in a diamond-Ge matrix already 30 years ago [31–33]. More recently, room temperature nanoindentation [34] and ultraviolet laser ablation at low pressure [35,36] have been employed to obtain hexagonal phases of Ge. Similarly to the case of Si, different routes toward hexagonal Ge nanowires have been explored [20,37–40]. Other hexagonal polytypes besides $2H$, e.g., $4H$ Ge, have also been reported [41–44].

Although hexagonal polytypes such as $2H$ and $4H$ of Si and Ge are well documented experimentally, little is known from theoretical studies about their electronic properties in comparison with the abundant literature for SiC (see, e.g., Ref. [45]). One publication [46] addresses their structural, cohesive, and electronic properties in the framework of the density functional theory (DFT) [47,48] with the local density approximation (LDA) [48] for the exchange-correlation (XC) functional. The $2H$ phases of Si and Ge have been recently investigated in detail, including elastic properties,
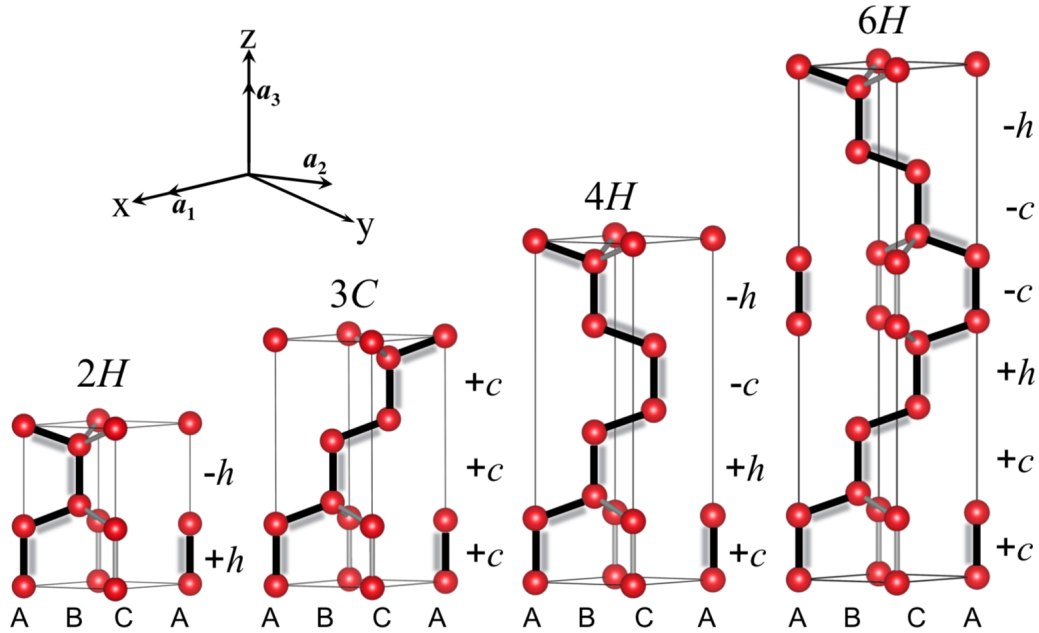
FIG. 1. Bond stacking along the [0001] direction in the hexagonal unit cells of the four polytypes. Group-IV atoms are displayed as red spheres. Bonds in the $(11\bar{2}0)$ plane are indicated by thick black lines. The cubic (c) or hexagonal (h) character of each bilayer is defined by the nonparallel bond in the plane. The signs $+$ and $-$ denote the orientation of the bilayer. For a more detailed explanation, see Ref. [45]. The primitive basis vectors $\boldsymbol{a}_i$ ($i = 1, 2, 3$) are also shown.

with DFT calculations using advanced XC functionals for improved band structures [49–51]. In fact, the Kohn-Sham band structures obtained from standard functionals in the LDA or generalized gradient approximation (GGA) drastically underestimate the fundamental gaps and interband energies of semiconductors [52], and germanium is wrongly predicted to be metallic independently of the polytype [46,53]. Accurate quasiparticle (QP) band structures can be obtained, for instance, within the GW approximation to the XC self-energy [52]. For $2H$-Si, such GW calculations are available [49]. It has, however, been shown that more efficient computational approaches allow one to obtain QP band structures of the same quality at a lower computational cost [50,54–56]. The most reliable such approaches consist in applying hybrid XC functionals, e.g., the Heyd-Scuseria-Ernzerhof (HSE06) functional [57] or a meta-GGA XC functional called MB-JLDA [55,58,59]. The MBJLDA functional is based on a modified Becke-Johnson (MBJ) exchange potential [60–62] together with LDA correlation. We note that an empirical-pseudopotential method (EPM) has also been applied in the literature to the $2H$ polytypes [63–65].

In this paper, we present a comprehensive overview of calculations for ground-state and excited-state properties of $2H$, $4H$, and $6H$ hexagonal polytypes of the group-IV elements Si and Ge. We include also calculations for the $3C$ diamond phase, using a nonprimitive hexagonal unit cell to facilitate the comparison. Concerning the ground state, we discuss atomic structures, phase stability, and elastic coefficients. In contrast to the 2002 work of Raffy, Furthmüller, and Bechstedt [46], where the LDA was employed, we use here the GGA Perdew-Burke-Ernzerhof XC functional revised for solids (PBEsol) [66]. The excellent accuracy of this functional for geometry optimization and calculation of elastic properties is proved in Ref. [50] for the $3C$ and $2H$ phases of Ge. Among

the excited-state properties we focus on the modification of band structures and band gaps with hexagonality. These band structures are now calculated with the HSE06 and MBJLDA functionals, which yield band structures in close agreement with experimental data for the most studied $3C$ and $2H$ phases [49,50]. In contrast to earlier LDA and GGA calculations, and in agreement with experiment, we obtain with these functionals an open band gap for all Ge polytypes. Taking advantage of the accuracy of our band gap calculations, we calculate branch-point energies and apply them to obtain band alignments at the interface between different polytypes.

II. THEORETICAL AND COMPUTATIONAL METHODS

A. Structural properties

All calculations were performed with the Vienna *ab initio* simulation package (VASP) [67,68]. The wave functions and pseudopotentials are described within the projector-augmented wave method [69] and the shallow Ge $3d$ electrons are considered as valence electrons. The plane-wave expansion is restricted to a cutoff of 500 eV. The Brillouin zone (BZ) integrations are carried out by means of Γ-centered $12 \times 12 \times M$ **k**-point meshes according to Monkhorst and Pack [70]. The value of M is varied according to the number of bilayers $p = 2, 3, 4, 6$ (see Fig. 1) in the unit cell. Explicitly, we use $M = 6, 4, 3, 2$ for the $2H$, $3C$, $4H$, and $6H$ phases. We apply the GGA PBEsol XC functional [66], a modified version of the Perdew-Burke-Ernzerhof (PBE) functional [71] optimized for solids, for structural optimizations. The lattice relaxation leads to a minimization of the total energy E_{tot} with a convergence accuracy of 1 meV/atom. The atomic geometry of the hexagonal polytypes pH are characterized by lattice constants a and c and $(p - 1)$ internal-cell parameters. The constants a and c give the cell volume $V = \sqrt{3}a^2c/2$ as well

TABLE I. Equilibrium structural parameters and total energies (relative to the energy of the 3C phase). A comparison with experimental and other theoretical values is also given.

Element	Polytype	a (Å)	$2c/p$ (Å)	$2c/pa$	V (Å^3/atom pair)	B_0 (GPa)	B_0'	E_{tot} (meV/atom)	Ref.
Si	2H	3.826	6.327	1.654	40.109	93.5	4.25	9.7	This paper
		3.824	6.257	1.6362	39.619				[18] (expt.)
		3.8237	6.3237	1.6538	40.035				[20] (expt.)
		3.837	6.317	1.646	40.271				[76] (expt.)
		3.840	6.280	1.630	40.098				[13] (expt.)
		3.798	6.280	1.653	39.226	96.7	4.06	10.7	[46] (theor.)
		3.828	6.325	1.652	40.133	92.8	4.24		[49] (theor.)
		3.800	6.270	1.650	39.204			11.7	[77] (theor.)
	4H	3.834	6.298	1.643	40.095	93.6	4.25	2.5	This paper
		3.837	6.293	1.640	40.126				[78] (expt.)
		3.840	6.270	1.633	40.034				[79] (expt.)
		3.806	6.254	1.643	39.228	96.7	4.13	2.4	[46] (theor.)
	6H	3.837	6.290	1.639	40.106	93.5	4.25	1.2	This paper
		3.810	6.244	1.639	39.248	96.7	4.13	1.0	[46] (theor.)
	3C	3.844	6.277	1.633	40.152	93.5	4.25	0.0	This paper
		3.840	6.272	1.633	40.047	97.9	4.24	0.0	[80] (expt.)
		3.816	6.230	1.633	39.283	96.6	4.18	0.0	[46] (theor.)
Ge	2H	3.993	6.589	1.650	45.493	63.7	4.99	16.0	This paper
		3.96	6.57	1.659					[31] (expt.)
		3.988	6.578	1.649					[39] (expt.)
		3.962	6.538	1.650	44.440	72.8	4.74	16.1	[46] (theor.)
		3.996	6.590	1.649	45.566	67.6	4.81	10.0	[50] (theor.)
		3.989	6.582	1.650	45.351	72.0			[55] (theor.)
	4H	4.001	6.568	1.642	45.516	67.2	4.75	7.1	This paper
		3.990	6.558	1.643	45.205				[43] (expt.)
		3.969	6.516	1.642	44.447	72.8	4.77	6.9	[46] (theor.)
	6H	4.004	6.560	1.638	45.535	67.2	4.67	4.5	This paper
		3.972	6.510	1.640	44.473	72.8	4.77	4.3	[46] (theor.)
	3C	4.010	6.550	1.634	45.596	66.0	4.08	0.0	This paper
		4.001	6.534	1.633	45.292	77.0	4.60	0.0	[80] (expt.)
		3.979	6.496	1.633	44.534	72.5	4.80	0.0	[46] (theor.)

as the cell shape by their ratio c/a. In the case of 3C in Fig. 1 this ratio is fixed as $2c/3a = \sqrt{8/3}$. The optimization of the atomic positions in the unit cell is important as demonstrated for III-V compounds [72]. Small deformations of the equilibrium atomic geometry are applied to extract elastic constants from the corresponding total energy variations. The Murnaghan equation of state (EOS) [73] $E_{tot} = E_{tot}(V)$ is applied to determine the equilibrium volume V_0, the isothermal bulk modulus B_0, and its pressure derivative B_0'.

B. Electronic states

In order to compute approximate QP band structures, we apply two approaches based on approximations of more advanced treatments of the XC effects, the MBJLDA meta-GGA functional [60–62] and the HSE06 hybrid functional [57]. Spin-orbit coupling (SOC) is taken into account for all calculations. To perform hybrid functional calculations, we slightly reduce the density of the **k**-point meshes to $8 \times 8 \times M$, where $M = 6$ for 2H, $M = 4$ for 3C, $M = 3$ for 4H, and $M = 2$ for 6H polytypes. In the case of calculations with the meta-GGA functional, the cutoff energy was increased to 520 eV. The eigenvalues of the parity operator were calculated using the code IRREP [74,75].

III. RESULTS FOR GROUND-STATE PROPERTIES

A. Structural parameters

The calculated lattice parameters a and c of the hexagonal Bravais lattices (as well as of the diamond lattices in their hexagonal unit cells), together with their ratio c/a and the cell volume V, are listed in Table I. Therein, the lattice constant c is divided by the number of bilayers p in the unit cell, and the volume per atom pair is calculated as $V = \sqrt{3}a^2c/(2p)$. We can observe clear trends with the hexagonality h, where $h = 1.00$ for the 2H polytype, 0.50 for the 4H polytype, 0.33 for the 6H polytype, and 0.00 for the 3C polytype, as indicated in Fig. 1.

For both Si and Ge the lattice constant a decreases, while the normalized lattice constant $2c/p$ and the ratio $2c/(pa)$ increase with increasing hexagonality [see Fig. 2(a)]. The trend observed for a also holds for the volume per atom in the Ge case. However, for Si the trend is not monotonous, because of the opposite behavior of a and $2c/p$. The cell volume V reaches a minimum at $h = 0.50$, i.e., for the 4H-Si polytype. The general trend with respect to h indicates an increasing deformation of the tetrahedral units that are stretched along the c axis.

Our findings in Table I are in qualitative agreement with other calculations and experimental data. However,
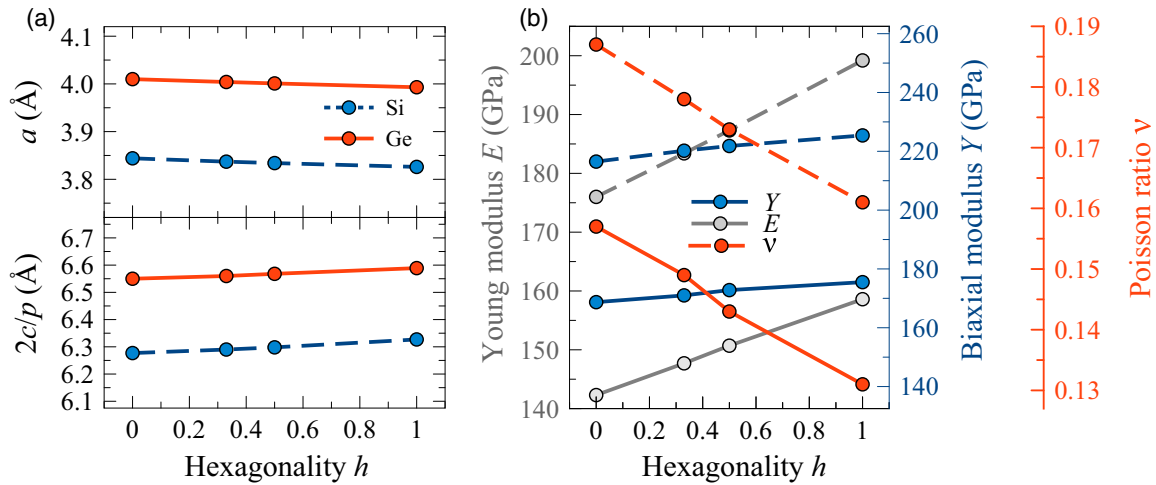
FIG. 2. Dependence on the hexagonality of (a) structural and (b) elastic properties of Si (dashed lines) and Ge (solid lines) polytypes.

systematic experimental studies are missing. The theoretical data obtained in the framework of DFT-LDA [46] show exactly the same qualitative behavior not only for Si and Ge, but also for SiC [81]. The underestimation of a, $2c/p$, and V in Ref. [46] is a consequence of the well-known tendency of the LDA functional to overbind [82]. The computed DFT-PBEsol lattice constants are much closer to the measured a and c values, clearly indicating the improved quality of the PBEsol XC functional. For all hexagonal polytypes the $2c/(pa)$ ratio is larger than the ideal value $\sqrt{8/3} = 1.633$ of the $3C$ polytype. This result agrees with observations for III-V and II-VI compounds that crystallize in the zinc blende structure under ambient conditions [77,83]. By contrast, the ratio $2c/(pa)$ of compounds such as III-nitrides, SiC, and some II-VI materials, for which the wurtzite $2H$ polytype is more stable than $3C$, is below the ideal value [45,77,83].

Our results for the fits to the Murnaghan EOS are also displayed in Table I. The overall elastic properties expressed by the isothermal bulk modulus B_0 and its pressure derivative B_0' remain practically uninfluenced by the polytype geometry in the case of Si. Because of the shallow Ge $3d$ core electrons, minor deviations appear for Ge. The B_0' values slightly increase with h, while B_0 exhibits a weakly pronounced maximum for intermediate hexagonality values. Similar trends are observed using the DFT-LDA approximation [46]. However, due to the overbinding tendency of LDA, the B_0 values are systematically larger by about 3–4% in comparison to the DFT-PBEsol results.

B. Energetics

In Table I we list the total energy differences between the energies of the polytypes and the energy of the $3C$ structure. We can see that diamond $3C$ is the most stable polytype for both Si and Ge, in agreement with experiments. This crystal structure is followed by $6H$ and $4H$, whereas the lonsdaleite geometry $2H$ is substantially higher in energy. We conclude that the general trend is an increase in the internal energy with hexagonality. There is, however, a substantial difference between Si and Ge: For the former the energy increase with hexagonality can be fitted with an exponential curve, while the

growth is only approximately linear for Ge [see Fig. 3(a)]. The absolute values of the energy differences calculated with the PBEsol density functional are close to the DFT-LDA energies of Ref. [46]. Our result for the $2H$-$3C$ energy difference for the Si case is also close to the value reported by Yeh *et al.* [77].

The polytypes differ only in the stacking sequence of the bonding tetrahedra along the c axis. We can therefore model the internal energy of a generic polytype using a one-dimensional Ising-type model, called the axial next-nearest-neighbor Ising (ANNNI) model [84], that uses three parameters J_j ($j = 1, 2, 3$) to account for the jth-neighbor bilayer interaction. This model can be successfully applied to explain the energy differences in Table I [45,46,83–85]. The parameters of the model and the resulting stacking-fault energies are summarized in Table II. The ANNNI parameters allow the construction of a polytypic phase diagram in terms of the relative interaction strengths J_1/J_2 and J_3/J_2. Our
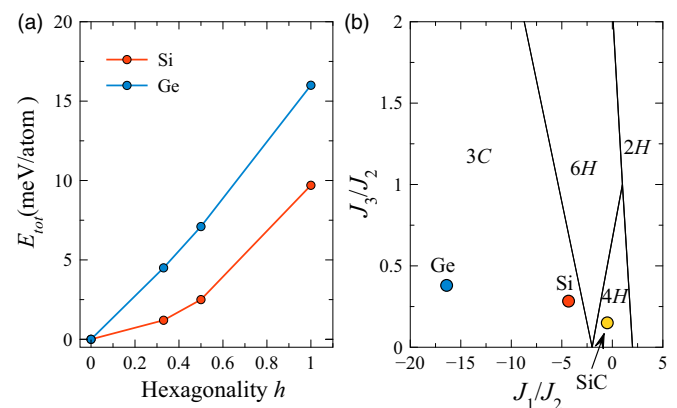
FIG. 3. (a) Total energies of the polytypes vs hexagonality with respect to $3C$. (b) Phase diagram of polytypes from the ANNNI model. The solid lines represent the phase boundaries between the parameter regions where the indicated phases are the most stable. The blue and red dots represent the group-IV materials that favor the $3C$ polytype. For comparison the $4H$ equilibrium structure of SiC [45] is also displayed.

TABLE II. Parameters J_j of the ANNNI model (in meV/group-IV pair) and resulting stacking-fault energies γ (in mJ/m^2). Note that it is hard to extract precise data for the different types of stacking faults from experiments.

Element	J_1	J_2	J_3	γ_{ISF}	γ_{ESF}	γ_{TSF}	Ref.
Si	10.4	−2.4	−0.68	36.5	21.2	8.9	This paper
	11.4	−2.9	−0.75	39.3	20.6	8.4	[46] (theor.)
				69	60		[92] (expt.)
				55 ± 7			[93] (expt.)
Ge	16.4	−1.0	−0.38	69.4	63.3	30.8	This paper
	16.5	−1.2	−0.46	69.7	62.2	30.0	[46] (theor.)
				60 ± 10			[93] (expt.)

TABLE III. Internal-cell parameters for unit cells of type pH in relative coordinates (fraction of the c parameter, units of 10^{-4}) with respect to the lowest atom in the cell, whose internal parameter is set to zero. For comparison, DFT-LDA values from Ref. [46] are also listed.

	2H	4H			6H				
Element	$\varepsilon(1)$	$\varepsilon(1)$	$\varepsilon(2)$	$\delta(2)$	$\varepsilon(1)$	$\varepsilon(2)$	$\varepsilon(3)$	$\delta(2)$	$\delta(3)$
Si									
This paper	−10.0	6.6	−1.7	8.3	6.2	3.3	−1.2	7.4	2.9
Ref. [46]	−9.4	6.6	−1.9	8.5	6.6	3.6	−1.2	7.8	2.9
Ge									
This paper	−7.2	7.4	−2.1	9.5	6.8	3.6	−1.5	8.3	3.2
Ref. [46]	−7.0	8.0	−1.7	9.7	7.1	4.0	−1.4	8.5	3.1

phase diagram for $3C$, $6H$, $4H$, and $2H$ polytypes is shown in Fig. 3(b). We indicate in the different parameter regions which is the most stable phase. The solid lines represent phase boundaries. This figure clearly shows that under ambient conditions, Si and Ge crystallize in the diamond structure. However, the corresponding coordinate point $(J_1/J_2, J_3/J_2)$ is much closer for Si diamond than for Ge diamond to the $3C$-$6H$ phase boundary with $J_1 + 2J_2 + 3J_3 = 0$ and the triple point $J_1 = -2J_2$ of the three polytypes $3C$, $6H$, and $4H$. The reason for this is the larger (smaller) nearest-neighbor interaction J_1 (second-nearest-neighbor interaction J_2) in Ge (Si) (see Table II). This phase diagram suggests that under near-equilibrium conditions the preparation of hexagonal polytypes should be easier for Si. In fact, the position of the diamond structure in the Si phase diagram is similar to that of the ground-state $4H$ in the phase diagram of SiC, a compound which shows a pronounced polytypism [45,86].

By using the ANNNI model, not only can the different polytypes be easily characterized, but also the formation of a stacking fault, i.e., a two-dimensional (2D) defect with respect to the infinite stacking in the $3C$ structure, can be studied with this simple model. The most common stacking faults are the intrinsic stacking fault (ISF), the extrinsic stacking fault (ESF), and the twin stacking fault (TSF) [87–91]. The ISF (ESF) is defined by removing (adding) one bilayer from (to) the $3C$ stacking sequence. A TSF defect occurs if a reflection symmetry is present with the mirror plane positioned in the middle of the bilayer. The corresponding formation energies (per atom) are given as [89,91]

$$E_f(\text{ISF}) = 4(J_1 + J_2 + J_3),$$
$$E_f(\text{ESF}) = 4(J_1 + 2J_2 + 2J_3),$$
$$E_f(\text{TSF}) = 2(J_1 + 2J_2 + 3J_3). \quad (1)$$

The stacking-fault energies γ per unit area can be calculated by dividing the formation energies of (1) by the area $\sqrt{3}a^2/2$ of the hexagonal unit cell in the (111) or (0001) plane. The resulting values are also listed in Table II.

These formation energies depend very weakly on the XC functional. However, they significantly depend on the chemical element. The theoretical values indicate that the stacking-fault generation is less energy expensive in Si than in Ge, while the experimental formation energies are rather similar. It is known from experiments that Si films crystallized

with pulsed laser beams show many extrinsic stacking faults [28,94].

C. Internal-cell parameters

The atomic positions in the unit cell of a pH polytype are not only defined by the lattice constants a and c, which fix the primitive basis vectors of the Bravais lattice $\boldsymbol{a}_1 = a(1, 0, 0)$, $\boldsymbol{a}_2 = \frac{a}{2}(-1, \sqrt{3}, 0)$, and $\boldsymbol{a}_3 = c(0, 0, 1)$, but also defined by the internal-cell parameters. The stackings in Fig. 1 can be described as $ABABABABABAB\cdots$ for $2H$, $ABCABCABCABC\cdots$ for $3C$, $ABCBABCBABCB\cdots$ for $4H$, and $ABCACBABCACB\cdots$ for $6H$. The letters indicate the location of the vertical bonds (indicated with thick black lines in Fig. 1) in the layers stacked along z in the unit cell. The lowest atom sets the origin $(0,0,0)$, and the other atoms in the vertical bonds have Wyckoff positions [95] $(0, 0, u)$, $(1/3, 2/3, v)$, and $(2/3, 1/3, w)$ with

$$2H\colon \quad u_L = 0, \quad u_U = \tfrac{3}{8} + \varepsilon(1),$$
$$4H\colon \quad u_L = 0, \quad u_U = \tfrac{3}{16} + \varepsilon(1),$$
$$v_L = \tfrac{1}{4} + \delta(2), \quad v_U = \tfrac{7}{16} + \varepsilon(2),$$
$$6H\colon \quad u_L = 0, \quad u_U = \tfrac{1}{8} + \varepsilon(1),$$
$$v_L = \tfrac{1}{4} + \delta(2), \quad v_U = \tfrac{7}{24} + \varepsilon(2),$$
$$w_L = \tfrac{1}{3} + \delta(3), \quad w_U = \tfrac{11}{24} + \varepsilon(3), \quad (2)$$

where the deviations of the atomic positions from the ideal ones are given by the dimensionless internal-cell parameters $\varepsilon(1), \ldots, \varepsilon(p/2)$ for the upper (U) atom in the bilayer and $\delta(1) = 0, \ldots, \delta(p/2)$ for the lower (L) atom.

Table III shows that the geometry optimization produces only small deviations from the ideal lattice positions. The discrepancies of the relative site positions between Si and Ge pH polytypes are rather small, whereas the absolute shifts are much larger because of the different values of the lattice constant c (see Table I). The values calculated with the PBEsol and LDA functionals are also very similar.

The largest deviations happen for the $2H$ lonsdaleite polytype. However, even for $2H$ the resulting $u = 3/8 + \varepsilon(1)$ parameter is still very close to the ideal value $u = 0.375$, in agreement with previous computations (see, e.g., Refs. [49,50,77]).

TABLE IV. Elastic stiffness constants C_{ij}, bulk modulus B_0, Young's modulus E, biaxial modulus Y (all in GPa), and Poisson ratio ν (dimensionless). We compare the calculated values with reported theoretical values for $2H$ and experimental values for $3C$.

Element	Polytype	$C_{11}+C_{12}$	C_{11}	C_{12}	C_{13}	C_{33}	C_{44}	B_0	E	Y	ν	Ref.
Si	$2H$	239.5	185.6	53.9	38.6	211.6	43.8	93.8	199.2	225.4	0.161	This paper
		237.0			37.0	213.0			202.0	224.0	0.157	[49]
		230.8	181.9	48.9	33.3	205.9	48.9	88.9			0.213	[99]
		239.0	185.0	54.0	38.0	211.0	47.0	94.0	198.0	225.0	0.159	[100]
		249.3	194.0	55.3	42.0	206.5	44.8	97.0	192.3	232.2	0.168	[97]
	$4H$	238.8	183.4	55.4	41.4	201.7	50.9	93.9	187.3	221.8	0.173	This paper
			179.9	50.2	36.0	197.1	52.2	89.1			0.214	[99]
	$6H$	238.3	182.5	55.8	42.4	198.5	53.2	93.9	183.4	220.2	0.178	This paper
			179.1	50.3	36.9	194.1	53.7	88.9			0.214	[99]
	$3C$	237.0	183.4	53.6	44.4	192.7	56.0	93.8	176.0	216.5	0.187	This paper
		248.8	191.4	57.4	44.8	204.0	57.9	97.9	203.6	248.4	0.180	[97]
Ge	$2H$	182.5	143.1	39.3	23.9	164.9	40.1	69.5	158.6	175.5	0.131	This paper
		177.7	124.0	53.7	22.8	159.4	39.1	67.3	153.5	171.2	0.128	[51]
		193.1	155.6	37.5	27.7	169.3	41.1	74.0	161.4	184.0	0.143	[97]
		179.0	138.0	41.0	25.0	161.0	38.0	77.0	154.0	171.0	0.140	[100]
	$4H$	181.3	141.2	40.0	25.9	158.1	42.0	69.4	150.7	172.8	0.143	This paper
	$6H$	180.3	141.4	38.8	26.8	155.7	43.0	69.3	147.7	171.0	0.149	This paper
	$3C$	179.3	142.7	36.6	28.2	151.2	44.9	69.2	142.3	168.7	0.157	This paper
		183.3	154.2	35.3	23.3	159.9	47.6	68.9	154.0	176.5	0.127	[101]

D. Elastic coefficients

The elastic stiffness constants C_{ij} of the hexagonal polytypes pH ($p = 2, 4, 6$) and the $3C$ polytype in a hexagonal unit cell are extracted using DFT total energy calculations and the expression of the elastic energy for five different deformations ($<1\%$) of the crystal lattice. Combinations of C_{ij} [96,97] yield the bulk modulus [51,98]

$$B_0 = \frac{(C_{11} + C_{12})C_{33} - 2(C_{13})^2}{(C_{11} + C_{12}) + 2(C_{33} - 2C_{13})}, \qquad (3)$$

the Young's modulus E, the biaxial modulus Y, and the Poisson ratio ν [51,98]

$$E = C_{33} - \frac{2(C_{13})^2}{C_{11} + C_{12}},$$

$$Y = C_{11} + C_{12} - \frac{2(C_{13})^2}{C_{33}}, \qquad (4)$$

$$\nu = \frac{C_{33}}{C_{11} + C_{12}}. \qquad (5)$$

The calculated results are listed in Table IV. We can compare the elastic constants of the lonsdaleite polytype with data computed recently within similar approaches and XC functionals [49,97,100]. In the case of $2H$-Ge, calculations [51] performed with the ELASTIC code [102], based on VASP total energies, are also available. For $3C$ we reexpress the stiffness constants [101] measured for the cubic system to obtain the coefficients corresponding to the hexagonal symmetry applying the formulas (including corrections) given in Ref. [103]. Apart from the almost constant isothermal bulk modulus B_0 and the hardly varying stiffness constant C_{12}, the other elastic constants show clear trends with hexagonality h. We observe an increasing trend with hexagonality h for

$C_{11} + C_{12}$, C_{11}, C_{33}, E, and Y and a decreasing trend for C_{13}, C_{44}, and ν. The almost linear dependence with respect to the parameter h is displayed in Fig. 2(b) for E, Y, and ν. The dependence of the crystal stiffness on hexagonality is related to the different tetrahedron deformation and stacking. Of course, in comparison, variations of elastic properties due to the presence of a different chemical element, Si or Ge, are much stronger than effects related to the different polytype. This is especially visible in the values of the bulk modulus B_0 or of the reciprocal compressibility, which varies slightly around 94 GPa for Si and 68 GPa for Ge. A similar effect of the chemistry is visible for the other elastic properties. Only the Poisson ratios $\nu = 0.161$–0.187 (Si) and $\nu = 0.131$–0.157 (Ge) versus decreasing h exhibit similar chemical and crystallographic ranges of variation.

For the polytype $2H$ the results can be compared with data from previous calculations [49,51,97,100]. We could verify an excellent agreement with stiffness constants and elastic moduli computed using the same or similar XC functionals in the GGA. If LDA functionals [97] are employed, the elastic constants are systematically larger, in agreement with the tendency for overbinding of the LDA. For a detailed comparison, all values can be found in Table IV.

Experimental data are available for the $3C$ polytype [101]. We find qualitative agreement between measured and computed values, with overall smaller theoretical values, as expected due to the slight tendency of the PBEsol functional to underbind. Very recently, combining nanoindentation and *in situ* high-pressure synchrotron x-ray diffraction, the Young's modulus $E = 152.4$ GPa, the bulk modulus $B_0 = 91.8$ GPa, and the Possion ratio $\nu = 0.22$ of hexagonal silicon have been determined [104]. The deviations of E and ν from the calculated values in Table IV may be traced back to the polycrystalline nature of the samples.
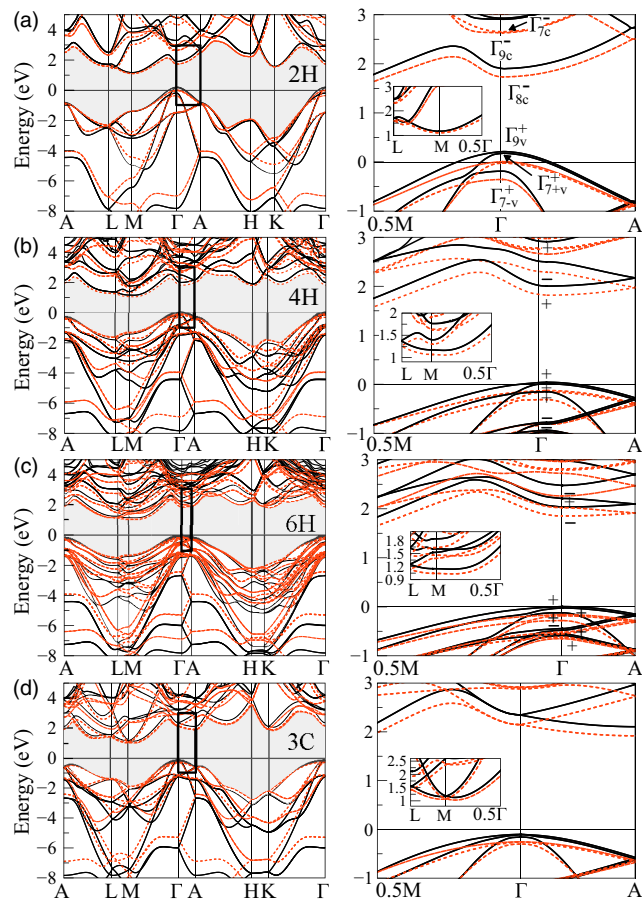
FIG. 4. Approximate QP band structures of the four Si polytypes (a) $2H$, (b) $4H$, (c) $6H$, and (d) $3C$ along high-symmetry lines, calculated within MBJLDA (red dashed lines) and HSE06 (black lines). The right panels show zooms on an energy interval around the fundamental gap and the BZ center, as indicated in the left panels by a black rectangle. The BP is used as energy zero, and BPs are indicated by black horizontal lines in the right panels of (b) and (c). The insets show the lowest conduction bands in MBJLDA and HSE06 on the Γ-M-L lines. The irreducible representations of high-symmetry states around the lowest conduction bands and highest valence bands are given in the double-group notation of Koster *et al.* [107] for $2H$. Because of zone-folding arguments the denotation of $2H$ is also applied in the cases of $4H$ and $6H$. *Ab initio* band parities at Γ are also displayed for all hexagonal polytypes. The gap regions are shaded in gray.

FIG. 5. Approximate QP band structures of the four Ge polytypes (a) $2H$, (b) $4H$, (c) $6H$, and (d) $3C$ along high-symmetry lines, calculated within MBJLDA (red dashed lines) and HSE06 (black lines). The right panels show zooms on an energy interval around the fundamental gap and the BZ center, as indicated in the left panels by a black rectangle. The BP is used as energy zero, and BPs are indicated by black horizontal lines in the right panels of (b) and (c). The insets show the lowest conduction bands in MBJLDA and HSE06 on the M-L line. The irreducible representations of the high-symmetry states around the lowest conduction bands and highest valence bands are given in the double-group notation of Koster *et al.* [107] for $2H$. Because of zone-folding arguments the denotation of $2H$ is also applied in the cases of $4H$ and $6H$. *Ab initio* band parities at Γ are also displayed for all hexagonal polytypes. The gap regions are shaded in gray.

IV. RESULTS FOR EXCITED-STATE PROPERTIES

A. Band structures

In Figs. 4 and 5 we display the electronic band structures of the four considered polytypes of Si and Ge. The electronic states are calculated using approximate QP frameworks, namely, the MBJLDA potential and the hybrid HSE06 functional. In the left panels the band energies are plotted along the high-symmetry lines A-L-M-Γ-A-H-K-Γ of the hexagonal BZ. In the right panels are zooms on the **k**-space region around Γ, along the ΓA and ΓM directions, and on energies around the gap. The insets display the lowest conduction bands outside Γ. For comparison, we also show the band

structure of the cubic polytype, folded in the hexagonal BZ, that results from the use of a nonprimitive hexagonal $3C$ unit cell, as illustrated in Fig. 1. The height of the different hexagonal BZs varies with the polytype, i.e., it is determined by the number of bilayers p along the c axis, whereas the in-plane hexagonal sections perpendicular to the c axis are basically equal.

In order to align the band structures of the different polytypes, we define the branch-point (BP) energy as the common energy zero. We compute the BP for each polytype applying an approximate treatment [105] that has been reliably tested to give excellent results for band discontinuities between semiconductors, their polytypes, and their alloys [83,105,106].

Following the procedure of Schleife *et al.* [105], we use $2p$ conduction and $4p$ valence bands to construct the approximate charge neutrality point. If only half of the bands are applied, the BP is shifted toward higher energies (see $2H$-Si and $2H$-Ge in Ref. [106]). The resulting eigenvalues, band parameters, and gaps are listed in Tables V and VI.

The energy levels can be labeled using the notation derived for lonsdaleite [107]. For the refinement of the representations we follow Refs. [63,64], where a conduction (valence) band state has the subscript c (v). All zone center states in $2H$ lonsdaleite with space group D_{6h}^4 belong to Γ_7, Γ_8, or Γ_9 representations with either even or odd parity because of the center of inversion symmetry. For all hexagonal polytypes, $2H$, $4H$, and $6H$, the band parities have been calculated as expectation values of the parity operator. They agree with other calculated values for $2H$-Ge [50] but disagree with the parities derived within the empirical-pseudopotential method (EPM) for both $2H$-Si and $2H$-Ge [65]. The irreducible representations of the space group at Γ are just the representations of the point group D_{6h}, i.e., all symmetry operations of the point group C_{6v} as well as the inversion. For **k** points out of Γ with a finite component along the c axis the little group is C_{6v}, i.e., a point on the Δ line, but recovers the point group D_{6h} at the A point. The little groups of the high-symmetry **k** points on the zone boundaries of the hexagonal BZ are D_{3h} for K and H but D_{2h} for L and M. Even including SOC, the bands in Figs. 4 and 5 remain twofold degenerate because of the inversion symmetry. Point group operations must be followed by appropriate fractional translations to obtain the irreducible representation of a wave function. Interestingly, not only at A and L but also along the L-M line, a couple of bands merge, so that, considering spin, a fourfold degeneracy appears. In the cubic case $3C$ we do not apply band labels of the $2H$ space group, despite the O_h^7 space group of the diamond geometry. Information on the irreducible representations of the band states of $2H$ considering the hexagonal crystal field and SOC can be found elsewhere [65].

The lonsdaleite $2H$ band structures are displayed in Figs. 4(a) and 5(a). The double-group notations of the irreducible representations of the band states are chosen according to Refs. [50,65] including the parity. The corresponding single-group notation for lonsdaleite without SOC can be found elsewhere [64,108,109]. Rules for the transition between single- and double-group notations, i.e., without and with SOC, for the C_{6v}^4 symmetry are listed in Refs. [110,111]. The most important band energies at Γ are made visible in the zoomed band structures of Figs. 4(a) and 5(a). They are listed together with the energies of the conduction band minimum (CBM) on the Γ-M-L lines for Si and the L-M line for Ge in Table V. The $2H$-Si crystal remains an indirect-gap semiconductor with the CBM near M and gap energy $E_g^{\mathrm{ind}}(\Gamma_{9v}^+ \to M_{5c}) = 1.10$ (0.98) eV according to MBJLDA (HSE06) calculations. In the following, all values will be given as MBJLDA (HSE06). While the lowest conduction band is an sp-derived Γ_8^- state in both $2H$ polytypes, the weaker SOC and stronger chemical bonding give rise in Si to p_{xy}-type second and third conduction bands, Γ_{9c}^- and Γ_{7c}^-, respectively, which only slightly split (by about 20 meV). In the case of Ge, instead, the second Γ_{7c}^- conduction band is mainly s derived. Such a pure s band occurs for Si at the

TABLE V. Energy eigenvalues (in eV) of the six lowest conduction bands (c) and three highest valence bands (v) at Γ obtained from MBJLDA (HSE06) calculations. Each level is twofold degenerate. The state parity (+ or −) is also listed. The BP is used as energy zero. Its energy distance from the VBM can be obtained from the eigenvalues of the highest valence band v_1.

Band	Si polytypes				Ge polytypes			
	2H	4H	6H	3C	2H	4H	6H	3C
c_6	4.835 (−) (5.249)	3.015 (−) (3.303)	2.847 (−) (3.123)	3.881 (4.200)	4.946 (−) (5.580)	2.910 (−) (3.448)	1.862 (+) (2.142)	3.003 (3.496)
c_5	4.329 (−) (4.780)	2.817 (−) (3.089)	2.823 (−) (3.098)	2.946 (3.231)	3.275(−) (3.765)	2.758(−) (3.281)	1.616 (−) (1.899)	3.003 (3.491)
c_4	3.014 (−) (3.297)	2.794 (−) (3.063)	2.718 (−) (2.977)	2.946 (3.219)	2.811 (−)(3.251)	1.592 (+) (1.872)	1.200 (−) (1.409)	2.807 (3.247)
c_3	2.656 (−) (2.930)	2.669 (+) (2.910)	2.256 (−) (2.476)	2.911 (3.186)	2.678 (−) (3.104)	1.262 (−) (1.522)	1.001 (+) (1.168)	1.106 (1.238)
c_2	2.634 (−) (2.902)	2.292 (−) (2.498)	2.030 (+) (2.210)	2.160 (2.346)	1.092 (−) (1.135)	1.011 (−) (1.212)	0.976 (−) (1.155)	1.105 (1.238)
c_1	1.735 (−) (1.903)	1.830 (+) (2.018)	1.860 (−) (2.035)	2.160 (2.345)	0.743 (−) (0.797)	0.807 (+) (1.009)	0.824 (+) (0.976)	0.930 (1.015)
v_1	0.008 (+) (0.212)	−0.126 (+) (0.042)	−0.160 (+) (0.004)	−0.255 (−0.102)	0.435 (+) (0.514)	0.338 (+) (0.441)	0.306 (+) (0.390)	0.240 (0.300)
v_2	−0.024 (+) (0.178)	−0.154 (+) (0.010)	−0.187 (+) (−0.024)	−0.255 (−0.102)	0.315 (+) (0.379)	0.261 (+) (0.376)	0.251 (+) (0.308)	0.236 (0.300)
v_3	−0.356 (+) (−0.146)	−0.301 (+) (−0.154)	−0.286 (+) (−0.122)	−0.302 (−0.156)	0.002 (+) (0.028)	0.001 (+) (0.083)	−0.004 (+) (0.008)	−0.032 (−0.016)

TABLE VI. Important conduction and valence band splittings, distances of the p lowest conduction bands, and direct and indirect gaps between conduction and valence bands (in eV). Values are obtained from calculations using MBJLDA (HSE06).

Material	Polytype	Δ_{cf}	Δ_{SO}	$\Delta_{SO\parallel}$	$\Delta_{SO\perp}$	$\Delta\varepsilon_c$	$E_g^{dir}(\Gamma)$	E_g^{ind} (near M)
Si	2H	0.345 (0.330)	0.050 (0.054)	0.050 (0.054)	0.053 (0.053)	0.899 (1.029)	1.728 (1.691)	1.096 (0.984)
	4H	0.156 (0.170)	0.048 (0.054)	0.048 (0.050)	0.047 (0.048)	0.965 (1.045)	1.955 (1.976)	1.233 (1.131)
	6H	0.104 (0.104)	0.048 (0.052)	0.048 (0.050)	0.048 (0.047)	0.986 (1.088)	2.021 (2.031)	1.247 (1.145)
	3C	0.000 (0.000)	0.047 (0.054)	0.047 (0.056)	0.046 (0.048)	0.752 (0.874)	2.415 (2.447)	1.291 (1.232)
Ge	2H	0.274 (0.299)	0.278 (0.317)	0.278 (0.332)	0.271 (0.320)	0.349 (0.338)	0.308 (0.283)	0.629 (0.615)
	4H	0.140 (0.145)	0.274 (0.310)	0.274 (0.280)	0.271 (0.306)	0.786 (0.863)	0.469 (0.568)	0.648 (0.750)
	6H	0.093 (0.102)	0.272 (0.314)	0.272 (0.362)	0.271 (0.317)	1.038 (1.166)	0.518 (0.586)	0.743 (0.769)
	3C	0.000 (0.000)	0.275 (0.316)	0.275 (0.323)	0.267 (0.308)	0.176 (0.223)	0.690 (0.715)	0.643 (0.690)

much higher energy of 2.6 eV above the lowest conduction band. In 2H-Si the direct gap at Γ, $E_g^{dir}(\Gamma_{9v}^+ \to \Gamma_{8c}^-) = 1.73$ (1.69) eV, is much larger. The second conduction band Γ_{9c}^- lies 2.63 (2.72) eV higher in energy. The situation is completely different in the 2H-Ge polytype, which becomes a direct-gap semiconductor with $E_g^{dir}(\Gamma_{9v}^+ \to \Gamma_{8c}^-) = 0.31$ (0.29) eV. The second conduction band $\Gamma_{7c}^- = 0.63$ (0.61) eV and the CBM $U_{5c} = 0.62$ (0.62) eV on the L-M line are somewhat higher in energy.

The uppermost valence bands Γ_{9v}^+, Γ_{7+v}^+, and Γ_{7-v}^+ are rather similar in 2H-Si and 2H-Ge. Only the larger SOC in Ge gives rise to larger energy splittings. Another interesting high-symmetry point is A, because of its possible mapping onto the Γ point or the A-Γ line in polytypes 4H, 6H, and 3C with larger unit cells and, therefore, less extended BZs in the direction of the c axis. The uppermost split valence bands $A_{8v} + A_{9v}$ and $A_{7v} + A_{9v}$ lie in Si and Ge below the interesting energy region of Γ_{9v}^+, Γ_{7+v}^+, and Γ_{7-v}^+. The lowest conduction band $A_{8c} + A_{7c}$, however, approaches the energy region of the second-lowest conduction band Γ_{9c}^- (Si) or Γ_{7c}^- (Ge). It will therefore influence the conduction bands in 4H and 6H according to folding arguments.

The most striking feature of the 4H, 6H, and 3C band structures in Figs. 4(b)–4(d) and 5(b)–5(d) is the increase in the number of bands according to the increase in the number of atoms in the unit cell. The bands surrounding the fundamental gap, e.g., the lowest conduction and highest valence bands, qualitatively show a similar behavior to those of the 2H polytypes. The three uppermost valence bands around Γ keep their symmetry, parity, and dispersion, independently of the polytype, since other valence bands cannot be folded in the same energy range. The lowest conduction band also maintains its similarity with the CBM at Γ with Γ_{8c}^- symmetry. The next conduction band minimum is found near M, along the M-L or M-Γ line. In the case of Si, the indirect CBM moves from M in the 2H phase toward a position along the Γ-M line, with an increasing distance from M with decreasing hexagonality. In the case of Ge the indirect minimum remains on the L-M line and does not show a unique trend with the hexagonality. This is mainly due to the mapping of the L point of the 2H crystal structure onto the M point in the 4H structure, and that of the 2H minimum near $\frac{1}{3}ML$ onto M in the BZ of 6H. The different behavior of the indirect CBM appears already in the diamond structure, where it occurs on

the Γ-X line near 0.8 ΓX for Si, but at the L point for Ge, where X and L are high-symmetry boundary points of the fcc BZ. The band folding, when going from 2H to 4H structures, and further to 6H, is also visible in the energy range of the lowest conduction bands near Γ. While in Ge the Γ_{8c}^- and Γ_{7c}^- band ordering of 2H is also preserved for 4H and 6H, in the two latter cases additional conduction bands appear in the corresponding energy region. For the 4H polytype, the two (SOC-split) lowest conduction bands at A of 2H appear in the energy region of the Γ_{8c}^- and Γ_{7c}^- bands. For 6H-Ge, four such bands mapped from the original A-Γ line can be found. Thereby, the lowest band state at $\frac{2}{3}A\Gamma$ in 2H is now folded onto Γ at an energy around the Γ_{8c}^- and Γ_{7c}^- bands. In any case, the lowest optical transition is parity forbidden for the 4H symmetry, in contrast to 2H and 6H. Therefore 4H-Ge should be not suitable for active optoelectronic applications.

In general, MBJLDA and HSE06 bands agree well near Γ and around the gap region. Farther away from the band gap the discrepancies become larger. For instance, while the three uppermost valence bands show excellent agreement, the lower valence bands are located at lower energies in the case of HSE06. This is due to the contribution of s orbitals to the lower valence bands and the stronger localization of s states using hybrid functionals [50].

B. Valence and conduction band parameters

From the MBJLDA (HSE06) band structures in Figs. 4 and 5 we can extract the band parameters and gaps in Tables V and VI. The six lowest conduction and highest three valence bands at Γ for the pH and 3C polytypes are listed in Table V. As energy zero we choose the BP. In the Si case the BP energy is slightly above the valence band maximum (VBM) in MBJLDA. Its distance from the VBM slightly increases with decreasing hexagonality, ranging from 0.008 to 0.255 eV, in good agreement with other studies and references therein [106]. Using the HSE06 functional, the BP position varies around the VBM. For 100% hexagonality it is 0.212 eV below the VBM, but it is 0.102 eV above the VBM in the 3C case. For Ge the BP is below the VBM, independent of the polytype and the approximate QP description. Its distance decreases from 0.435 (0.514) to 0.240 (0.300) eV with decreasing hexagonality of the polytype. Also this result is in good agreement with predictions in the literature for 2H-Ge
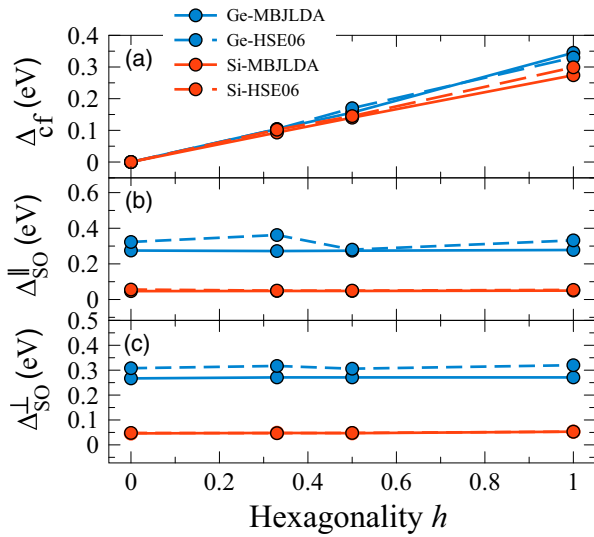
FIG. 6. Valence band parameters (a) Δ_{cf}, (b) $\Delta_{SO\parallel}$, and (c) $\Delta_{SO\perp}$ vs hexagonality of the polytypes in MBJLDA (solid lines) and HSE06 (dashed lines) for Si (red) and Ge (blue).

and 3C-Ge (see Ref. [105] and references therein). The absolute band positions at Γ with respect to the VBM in Table V are in agreement with similar calculations for 2H-Ge [50]. However, also the agreement with EPM calculations for 2H-Si and 2H-Ge is excellent [65], despite the use of completely different calculation methods.

From the valence band energies of Γ_{9v}^+, Γ_{7+v}^+, and Γ_{7-v}^+ in Table V we can extract the crystal-field splitting Δ_{cf} together with the spin-orbit splittings $\Delta_{SO\parallel}$ and $\Delta_{SO\perp}$ [112]. To this purpose, we apply formulas derived within the **k** · **p** theory [113]. The first values, Δ_{cf} and Δ_{SO}, are derived within the quasicubic approximation $\Delta_{SO\parallel} = \Delta_{SO\perp} = \Delta_{SO}$ [65,83]. The more general formulas, accounting also for the hexagonal anisotropy, are presented elsewhere [50,65,83]. The resulting values are listed in Table VI. Their trends with the hexagonality h of the polytype are displayed in Fig. 6. The hexagonal crystal field for the point group D_{6h} leads to a splitting of the threefold (sixfold with spin) degenerate Γ_{15} VBM of the original diamond structure (without SOC) into the $p_{x,y}$-derived Γ_6 and the p_z-derived Γ_1 levels, separated by Δ_{cf}. The crystal field displays an almost linear increase with the hexagonality, which is somewhat weaker for Si in comparison with Ge. The spin-orbit interaction gives rise to a further splitting of Γ_{6v} into Γ_{9v} and the Γ_{7+v} states, while the mixing with Γ_{1v} leads to Γ_{7-v}. An additional splitting Δ_{SO} occurs. In contrast to Δ_{cf}, the SOC splitting Δ_{SO} hardly varies with the hexagonality, because of its strong atomic character. We observe only a tendency toward a weak increase in the average SOC constant Δ_{SO} with the polytype hexagonality. The absolute values of Δ_{cf} and Δ_{SO} differ from those obtained with EPM for the 2H polytypes [65], because of the use of an ideal diamondlike atomic symmetry in the latter case. The anisotropy of the hexagonal polytypes leads to the introduction of two SOC constants, $\Delta_{SO\parallel}$ and $\Delta_{SO\perp}$ [113]. In Table VI we list the values resulting from the **k** · **p** formulas [112,113] by replacing Δ_{cf} with the value obtained in the quasicubic approximation. These values are also plotted in

Fig. 6. In general, the hexagonal splitting $\Delta_{SO\parallel} - \Delta_{SO\perp}$ is negligibly small and does not exhibit a unique trend with the hexagonality. In the case of 2H-Ge we find an anisotropy splitting of 7 meV, in agreement with other computations [50]. This splitting is of the order of 1 meV in the 2H-Si case.

Another interesting band parameter is the splitting of the p lowest conduction bands $\Delta\varepsilon_c$ at Γ, also listed in Table VI. Going down the rows for 2H, 4H, and 6H, there is a small increase with decreasing hexagonality for Si from 0.90 (1.03) to 0.99 (1.09) eV but a drastic variation from 0.35 (0.34) to 1.04 (1.17) eV for Ge. The 3C band splittings $\Delta\varepsilon_c = 0.75$ (0.87) eV (3C-Si) and 0.18 (0.22) eV (3C-Ge) do not follow the trends with hexagonality because of the more complex unfolding behavior when we compare the lowest conduction bands in the fcc BZ and the nonprimitive hexagonal BZ.

The direct gaps E_g^{dir} at Γ in Table VI also show a strong increase with decreasing hexagonality from 1.73 (1.69) to 2.42 (2.45) eV for Si and from 0.31 (0.28) to 0.69 (0.72) eV for Ge. This result is particularly important for Ge because its hexagonal polytypes are pseudodirect semiconductors, which have shown to be promising for applications in optoelectronics [39]. Only the 3C band structure displayed in the hexagonal BZ, in agreement with its well-known indirect character in the fcc BZ, exhibits a clear indirect behavior with the CBM near M. The calculated indirect gap is $E_g^{\text{ind}} = 0.64$ (0.69) eV. These values are close to the 0.65 (0.68) eV found for the indirect gap at the L point of the fcc BZ [50]. In the Si case the indirect gap slightly increases with decreasing hexagonality, going from 1.10 (0.98) to 1.29 (1.23) eV in MBJLDA (HSE06). Interestingly, the true lowest direct gap of 3C-Si appears somewhat outside Γ on the Γ-A line with a value of 2.17 (2.21) eV. Other HSE06 calculations [99] for the Si polytypes yield values for the indirect gap that are very similar to those in Table VI. Only the trend with the hexagonality is not unique. The gaps of 2H-Si obtained from *GW* calculations [49] are close to the values in Table VI. Optical measurements reveal that 4H-Si exhibits an indirect gap near 1.2 eV [78], in agreement with the first-principles calculations. In the case of hexagonal Si nanoribbons an indirect gap of 1.5 eV has been measured [29].

In the case of Ge, other HSE06 or even *GW* calculations give a slightly smaller direct gap at Γ, $E_g^{\text{dir}} = 0.23$ eV [114,115]. Band structure calculations with another hybrid exchange-correlation functional, the Becke three-parameter Lee-Yang-Parr (B3LYP) functional [43], deliver a much larger direct gap of $E_g^{\text{dir}} = 0.81$ eV for 4H-Ge. However, the B3LYP functional already tends to overestimate the gap of 3C-Ge. Measurements of bulk, unstrained 2H-Ge are difficult. Photoluminescence measurements on core-shell nanowires confirm a direct gap of about 0.3 eV [39]. Very recently, direct-band-gap features have been also observed by photoluminescence for hexagonal Ge nanostructures [116]. The measured direct gap of $E_g^{\text{dir}} = 0.8$ eV has been related to atomically thin hexagonal layers embedded in cubic germanium. The resulting carrier confinement and the compressive biaxial strain may explain the gap increase compared with the value of 0.3 eV calculated for a bulk, unstrained, hexagonal crystal.
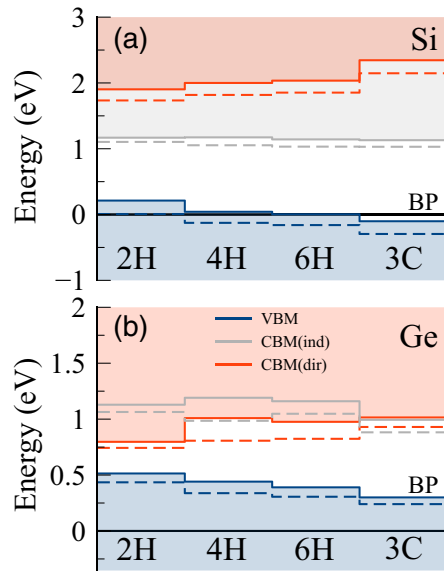
FIG. 7. Conduction [direct (dir) in red and indirect (ind) in gray] and valence (blue) band edges of hexagonal Si (a) and Ge (b) polytypes aligned by their branch-point energies (black horizontal lines). Dashed (solid) lines are computed using the MBJLDA (HSE06) functional.

C. Band discontinuities

Polytypic or heterocrystalline homojunctions have been observed in Si or Ge nanowires [38,114,117]. In particular, the $3C/2H$ homojunction has been studied, also theoretically [106,118]. The alignment of the band extrema by means of the BP energies in Table V allows us to determine the natural band discontinuities ΔE_c and ΔE_v for the homojunctions formed by two different polytypes of Si or Ge.

In Fig. 7(b) the situation for Ge is well defined because the enlargement of the direct gaps along $2H$, $4H$, $6H$, and $3C$ is distributed over both band edges, CBM and VBM. A heterocrystalline structure constituted by two different polytypes gives rise to a type-I heterostructure [96]. The natural band discontinuities can be extracted from Table V: $\Delta E_v = 0.10$ (0.10), 0.03 (0.05), 0.06 (0.09), 0.19 (0.21) eV and $\Delta E_c = 0.06$ (0.21), 0.02 (−0.03), 0.11 (0.04), 0.19 (0.22) eV for the junctions $2H/4H$, $4H/6H$, $6H/3C$, and $2H/3C$, respectively. The natural discontinuities $\Delta E_c = 0.19$ (0.22) eV and $\Delta E_v = 0.19$ (0.21) eV for the $2H/3C$ junction are in close agreement with results in the literature [106,108,114], even if they vary slightly with the numerical details of the calculation. The situation is less clear for the Si-based homojunctions displayed in Fig. 7(a). The natural band discontinuities between the VBMs are also well pronounced with $\Delta E_v = 0.12$ (0.17), 0.03 (0.03), 0.09 (0.10), 0.26 (0.31) eV for $2H/4H$, $4H/6H$, $6H/3C$, and $2H/3C$, while the conduction band minima are out of Γ and, moreover, only weakly vary. All the energies of the CBM are near the value 1.07 (1.15) eV above the BP. Consequently, in contrast to the holes, the electrons are hardly localized in real space in one of the considered Si-based homojunctions. For the homojunction $2H/3C$ we find $\Delta E_v =$

0.26 (0.31) eV and $\Delta E_c = -0.07$ (−0.04) eV, i.e., a tendency for a type-II heterocharacter [96]. This qualitative finding is in agreement with other theoretical predictions [106,118].

V. SUMMARY AND CONCLUSIONS

We investigated the properties of hexagonal polytypes of Si and Ge, a new class of recently synthesized group-IV materials, using state-of-the-art *ab initio* calculations. First, we discussed the structural, energetic, and elastic properties of the hexagonal polytypes $2H$, $4H$, and $6H$ of Si and Ge, in comparison with those of the energetically most favorable $3C$ diamond structure, obtained by applying density functional theory with the exchange-correlation potential PBEsol. The crystal structures, including internal degrees of freedom, and the elastic properties show clear trends with hexagonality. We compared our results with calculations in the literature performed with less accurate density functionals and with available measurements.

Some earlier surprising results on the energetics of the polytypes could be confirmed. The cubic $3C$ polytype is certainly the most stable for Si and Ge. The total energy of the pH polytypes increases with increasing hexagonality. The increase is larger for Ge than for Si. Consequently, the phase diagram constructed within a generalized Ising model shows Si to be much closer to the triple point of $3C$, $6H$, and $4H$ compared with Ge, indicating an easier production of the hexagonal polytypes in the case of Si, at least from the thermodynamic point of view. These results are consistent with the lower formation energies of stacking faults calculated for Si.

The different stacking of bonds in the polytypes affects the electronic properties. The direct (Si and Ge) gaps, as well as the indirect (Si only) gaps, decrease with increasing hexagonality. There is a clear tendency for Si to be an indirect semiconductor, regardless of crystal structure, while hexagonal Ge polytypes are direct semiconductors. This rule is slightly broken in the case of $3C$-Ge, where the lowest conduction band minima at Γ and outside Γ differ by only a few tenths of meV. The three uppermost valence bands are quite similar, regardless of the polytype. Only the size of the crystal field (Δ_{cf}) and spin-orbit splittings (Δ_{SO}) differ for Si and Ge. While Δ_{cf} varies almost linearly with the strength of the hexagonal crystal field, Δ_{SO} remains fairly constant for all polytypes.

The band alignment between Ge polytypes is particularly interesting, in view of the direct band gap, for applications in optoelectronics. We find that all heterostructures constituted by two polytypes of Ge have a type-I character, with electrons and holes confined in the layer with higher hexagonality. These results can suggest design rules for quantum-well light emitters.

ACKNOWLEDGMENT

[1] H. Olijnyk and W. B. Holzapfel, Phase transition in Si, Ge and Sn under pressure, J. Phys. Colloq. **45**, C8-153 (1984).

[2] J. Z. Hu, L. D. Merkle, C. S. Menoni, and I. L. Spain, Crystal data for high-pressure phases of silicon, Phys. Rev. B **34**, 4679 (1986).

[3] S. J. Duclos, Y. K. Vohra, and A. L. Ruoff, hcp to fcc transition in silicon at 78 GPa and studies to 100 GPa, Phys. Rev. Lett. **58**, 775 (1987).

[4] S. J. Duclos, Y. K. Vohra, and A. L. Ruoff, Experimental study of the crystal stability and equation of state of Si to 248 GPa, Phys. Rev. B **41**, 12021 (1990).

[5] M. I. McMahon and R. J. Nelmes, New high-pressure phase of Si, Phys. Rev. B **47**, 8337 (1993).

[6] J. Crain, G. J. Ackland, J. R. Maclean, R. O. Piltz, P. D. Hatton, and G. S. Pawley, Reversible pressure-induced structural transitions between metastable phases of silicon, Phys. Rev. B **50**, 13043 (1994).

[7] M. Hanfland, U. Schwarz, K. Syassen, and K. Takemura, Crystal Structure of the High-Pressure Phase Silicon VI, Phys. Rev. Lett. **82**, 1197 (1999).

[8] K. Takemura, U. Schwarz, K. Syassen, N. E. Christensen, M. Hanfland, D. L. Novikov, and I. Loa, High-pressure structures of Ge above 100 GPa, Phys. Status Solidi B **223**, 385 (2001).

[9] A. R. Verma and P. Krishna, *Polymorphism and Polytypism in Crystals* (Wiley, New York, 1966).

[10] W. Weltner, On polytypism and internal rotation, J. Chem. Phys. **51**, 2469 (1969).

[11] L. S. Ramsdell, Studies on silicon carbide, Am. Mineral. **32**, 64 (1947).

[12] S. Minomura and H. G. Drickamer, Pressure induced phase transitions in silicon, germanium and some III-V compounds, J. Phys. Chem. Solids **23**, 451 (1962).

[13] Y. Zhang, Z. Iqbal, S. Vijayalakshmi, and H. Grebel, Stable hexagonal-wurtzite silicon phase by laser ablation, Appl. Phys. Lett. **75**, 2758 (1999).

[14] V. Domnich, Y. Gogotsi, and S. Dub, Effect of phase transformations on the shape of the unloading curve in the nanoindentation of silicon, Appl. Phys. Lett. **76**, 2214 (2000).

[15] G. Viera, M. Mikikian, E. Bertran, P. Roca i Cabarrocas, and L. Boufendi, Atomic structure of the nanocrystalline Si particles appearing in nanostructured Si thin films produced in low-temperature radiofrequency plasmas, J. Appl. Phys. **92**, 4684 (2002).

[16] A. Fontcuberta i Morral, J. Arbiol, J. D. Prades, A. Cirera, and J. R. Morante, Synthesis of silicon nanowires with wurtzite crystalline structure by using standard chemical vapor deposition, Adv. Mater. **19**, 1347 (2007).

[17] P.-J. Alet, L. Yu, G. Patriarche, S. Palacin, and P. Roca i Cabarrocas, *In situ* generation of indium catalysts to grow crystalline silicon nanowires at low temperature on ITO, J. Mater. Chem. **18**, 5187 (2008).

[18] H. S. Ahn, S.-W. Kim, G. S. Lee, K. H. Kim, J. H. Lee, D. H. Ha, Y. T. Chun, and S. Ryu, Optical property of hexagonal (2H) silicon crystal, Semicond. Sci. Technol. **36**, 095023 (2021).

[19] F. J. Lopez, E. R. Hemesath, and L. J. Lauhon, Ordered stacking fault arrays in silicon nanowires, Nano Lett. **9**, 2774 (2009).

[20] H. I. T. Hauge, M. A. Verheijen, S. Conesa-Boj, T. Etzelstorfer, M. Watzinger, D. Kriegner, I. Zardo, C. Fasolato, F. Capitani, P. Postorino, S. Kölling, A. Li, S. Assali, J. Stangl, and E. P. A. M. Bakkers, Hexagonal silicon realized, Nano Lett. **15**, 5855 (2015).

[21] S. Dixit and A. K. Shukla, Optical properties of lonsdaleite silicon nanowires: A promising material for optoelectronic applications, J. Appl. Phys. **123**, 224301 (2018).

[22] S. Pandolfi, S. Zhao, J. Turner, P. Ercius, C. Song, R. Dhall, N. Menguy, Y. L. Godec, A. Courac, A. M. Minor, J. Eggert, and L. E. Dresselhaus-Marais, Multi-scale characterization of hexagonal Si-4H: A hierarchical nanostructured material, arXiv:2110.02943 [cond-mat.mtrl-sci].

[23] V. G. Eremenko and V. I. Nikitenko, Electron microscope investigation of the microplastic deformation mechanisms of silicon by indentation, Phys. Status Solidi A **14**, 317 (1972).

[24] P. Pirouz, R. Chaim, U. Dahmen, and K. H. Westmacott, The martensitic transformation in silicon—I. Experimental observations, Acta Metall. Mater. **38**, 313 (1990).

[25] U. Dahmen, K. H. Westmacott, P. Pirouz, and R. Chaim, The martensitic transformation in silicon—II. Crystallographic analysis, Acta Metall. Mater. **38**, 323 (1990).

[26] T. Y. Tan, H. Föll, and S. M. Hu, On the diamond-cubic to hexagonal phase transformation in silicon, Philos. Mag. A **44**, 127 (1981).

[27] H. Cerva, High-resolution electron microscopy of diamond hexagonal silicon in low pressure chemical vapor deposited polycrystalline silicon, J. Mater. Res. **6**, 2324 (1991).

[28] J. H. Kim and J. Y. Lee, Hexagonal silicon formation by pulsed laser beam annealing, Mater. Lett. **27**, 275 (1996).

[29] Y. Qiu, H. Bender, O. Richard, M.-S. Kim, E. Van Besien, I. Vos, M. de Potter de ten Broeck, D. Mocuta, and W. Vandervorst, Epitaxial diamond-hexagonal silicon nanoribbon growth on (001) silicon, Sci. Rep. **5**, 12692 (2015).

[30] G. Nicotra, C. Bongiorno, A. Convertino, M. Cuscunà, F. Martelli, and C. Spinella, Atomic structure of metal-free and catalyzed Si nanowires, MRS Online Proc. Libr. **1305**, 204 (2011).

[31] S.-Q. Xiao and P. Pirouz, On diamond-hexagonal germanium, J. Mater. Res. **7**, 1406 (1992).

[32] P. Pirouz, A. Garg, X. J. Ning, J. W. Yang, and S. Q. Xiao, High-temperature indentation of natural diamond and the quest for lonsdaleite, MRS Online Proc. Libr. **383**, 73 (1995).

[33] P. Müllner and P. Pirouz, A disclination model for the twin-twin intersection and the formation of diamond-hexagonal silicon and germanium, Mater. Sci. Eng. A **233**, 139 (1997).

[34] G. Dushaq, A. Nayfeh, and M. Rasras, Hexagonal germanium formation at room temperature using controlled penetration depth nano-indentation, Sci. Rep. **9**, 1593 (2019).

[35] Y. Zhang, Z. Iqbal, S. Vijayalakshmi, S. Qadri, and H. Grebel, Formation of hexagonal-wurtzite germanium by pulsed laser ablation, Solid State Commun. **115**, 657 (2000).

[36] B. Haberl, M. Guthrie, B. D. Malone, J. S. Smith, S. V. Sinogeikin, M. L. Cohen, J. S. Williams, G. Shen, and J. E. Bradby, Controlled formation of metastable germanium polymorphs, Phys. Rev. B **89**, 144111 (2014).

[37] N. Jeon, S. A. Dayeh, and L. J. Lauhon, Origin of polytype formation in VLS-grown Ge nanowires through defect generation and nanowire kinking, Nano Lett. **13**, 3947 (2013).

[38] L. Vincent, G. Patriarche, G. Hallais, C. Renard, C. Gardes, D. Troadec, and D. Bouchier, Novel heterostructured Ge

nanowires based on polytype transformation, Nano Lett. **14**, 4828 (2014).

[39] E. Fadaly, A. Dijkstra, J. R. Suckert, D. Ziss, M. van Tilburg, C. Mao, V. van Lange, K. Korzun, S. Kölling, M. Verheijen, D. Busse, C. Rödl, J. Furthmüller, F. Bechstedt, J. Stangl, J. Finley, S. Botti, J. E. M. Haverkort, and E. P. A. M. Bakkers, Direct-bandgap emission from hexagonal Ge and SiGe alloys, Nature **580**, 205 (2020).

[40] E. Scalise, A. Sarikov, L. Barbisan, A. Marzegalli, D. B. Migas, F. Montalenti, and L. Miglio, Thermodynamic driving force in the formation of hexagonal-diamond Si and Ge nanowires, Appl. Surf. Sci. **545**, 148948 (2021).

[41] E. López-Cruz and M. Cardona, Raman spectra of two new modifications of germanium: Allo-germanium and 4H-Ge, Solid State Commun. **45**, 787 (1983).

[42] J. R. Parsons and C. W. Hoelke, Crystallography of hexagonal germanium, Nature (London) **301**, 591 (1983).

[43] F. Kiefer, V. Hlukhyy, A. J. Karttunen, T. F. Fassler, C. Gold, E.-W. Scheidt, W. Scherer, J. Nylen, and U. Haussermann, Synthesis, structure, and electronic properties of 4*H*-germanium, J. Mater. Chem. **20**, 1780 (2010).

[44] G. Serghiou, N. Odling, H. J. Reichmann, G. Ji, M. Koch-Müller, D. J. Frost, J. P. Wright, R. Boehler, and W. Morgenroth, Hexagonal Si-Ge class of semiconducting alloys prepared by using pressure and low-temperature, Chem. Eur. J. **27**, 14217 (2021).

[45] F. Bechstedt, P. Käckell, A. Zywietz, K. Karch, B. Adolph, K. Tenelsen, and J. Furthmüller, Polytypism and properties of silicon carbide, Phys. Status Solidi B **202**, 35 (1997).

[46] C. Raffy, J. Furthmüller, and F. Bechstedt, Properties of hexagonal polytypes of group-IV elements from first-principles calculations, Phys. Rev. B **66**, 075201 (2002).

[47] P. Hohenberg and W. Kohn, Inhomogeneous electron gas, Phys. Rev. **136**, B864 (1964).

[48] W. Kohn and L. J. Sham, Self-consistent equations including exchange and correlation effects, Phys. Rev. **140**, A1133 (1965).

[49] C. Rödl, T. Sander, F. Bechstedt, J. Vidal, P. Olsson, S. Laribi, and J.-F. Guillemoles, Wurtzite silicon as a potential absorber in photovoltaics: Tailoring the optical absorption by applying strain, Phys. Rev. B **92**, 045207 (2015).

[50] C. Rödl, J. Furthmüller, J. R. Suckert, V. Armuzza, F. Bechstedt, and S. Botti, Accurate electronic and optical properties of hexagonal germanium for optoelectronic applications, Phys. Rev. Mater. **3**, 034602 (2019).

[51] J. R. Suckert, C. Rödl, J. Furthmüller, F. Bechstedt, and S. Botti, Efficient strain-induced light emission in lonsdaleite germanium, Phys. Rev. Mater. **5**, 024602 (2021).

[52] F. Bechstedt, *Many-Body Approach to Electronic Excitations: Concepts and Applications* (Springer-Verlag, Berlin, 2015).

[53] X. Cartoixa, M. Palummo, H. I. T. Hauge, E. P. A. M. Bakkers, and R. Rurali, Optical emission in hexagonal SiGe nanowires, Nano Lett. **17**, 4753 (2017).

[54] Z. Wang, Z. Zhang, S. Liu, J. Robertson, and Y. Guo, Electronic properties and tunability of the hexagonal SiGe alloys, Appl. Phys. Lett. **118**, 172101 (2021).

[55] N. Bao, F. Guo, D. Kang, Y. Feng, H. Wang, and J. Dai, Toward accurate electronic, optical and vibrational properties of hexagonal Si, Ge, and Si$_{1-x}$Ge$_x$ alloys from first-principle simulations, J. Appl. Phys. **129**, 145701 (2021).

[56] T. Kaewmaraya, L. Vincent, and M. Amato, Accurate estimation of band offsets in group IV polytype junctions: A first-principles study, J. Phys. Chem. C **121**, 5820 (2017).

[57] J. Heyd, G. E. Scuseria, and M. Ernzerhof, Hybrid functionals based on a screened Coulomb potential, J. Chem. Phys. **118**, 8207 (2003); Erratum: "Hybrid functionals based on a screened Coulomb potential" [J. Chem. Phys. 118, 8207 (2003)], **124**, 219906(E) (2006).

[58] M. Laubscher, S. Küfner, P. Kroll, and F. Bechstedt, Amorphous Ge quantum dots embedded in crystalline Si: *Ab initio* results, J. Phys.: Condens. Matter **27**, 405302 (2015).

[59] D. Waroquiers, A. Lherbier, A. Miglio, M. Stankovski, S. Poncé, M. J. T. Oliveira, M. Giantomassi, G.-M. Rignanese, and X. Gonze, Band widths and gaps from the Tran-Blaha functional: Comparison with many-body perturbation theory, Phys. Rev. B **87**, 075121 (2013).

[60] A. D. Becke and E. R. Johnson, A simple effective potential for exchange, J. Chem. Phys. **124**, 221101 (2006).

[61] F. Tran, P. Blaha, and K. Schwarz, Band gap calculations with Becke-Johnson exchange potential, J. Phys.: Condens. Matter **19**, 196208 (2007).

[62] F. Tran and P. Blaha, Accurate Band Gaps of Semiconductors and Insulators with a Semilocal Exchange-Correlation Potential, Phys. Rev. Lett. **102**, 226401 (2009).

[63] J. D. Joannopoulos and M. L. Cohen, Electronic properties of complex crystalline and amorphous phases of Ge and Si. I. Density of states and band structures, Phys. Rev. B **7**, 2644 (1973).

[64] J. D. Joannopoulos and M. L. Cohen, Electronic properties of complex crystalline and amorphous phases of Ge and Si. II. Band structure and optical properties, Phys. Rev. B **8**, 2733 (1973).

[65] A. De and C. E. Pryor, Electronic structure and optical properties of Si, Ge and diamond in the lonsdaleite phase, J. Phys.: Condens. Matter **26**, 045801 (2014).

[66] J. P. Perdew, A. Ruzsinszky, G. I. Csonka, O. A. Vydrov, G. E. Scuseria, L. A. Constantin, X. Zhou, and K. Burke, Restoring the Density-Gradient Expansion for Exchange in Solids and Surfaces, Phys. Rev. Lett. **100**, 136406 (2008).

[67] G. Kresse and J. Furthmüller, Efficient iterative schemes for *ab initio* total-energy calculations using a plane-wave basis set, Phys. Rev. B **54**, 11169 (1996).

[68] G. Kresse and J. Furthmüller, Efficiency of ab-initio total energy calculations for metals and semiconductors using a plane-wave basis set, Comput. Mater. Sci. **6**, 15 (1996).

[69] G. Kresse and D. Joubert, From ultrasoft pseudopotentials to the projector augmented-wave method, Phys. Rev. B **59**, 1758 (1999).

[70] H. J. Monkhorst and J. D. Pack, Special points for Brillouin-zone integrations, Phys. Rev. B **13**, 5188 (1976).

[71] J. P. Perdew, K. Burke, and M. Ernzerhof, Generalized Gradient Approximation Made Simple, Phys. Rev. Lett. **77**, 3865 (1996).

[72] C. Panse, D. Kriegner, and F. Bechstedt, Polytypism of GaAs, InP, InAs, and InSb: An *ab initio* study, Phys. Rev. B **84**, 075217 (2011).

[73] F. D. Murnaghan, The compressibility of media under extreme pressures, Proc. Natl. Acad. Sci. USA **30**, 244 (1944).

[74] M. Iraola, J. L. Manes, B. Bradlyn, T. Neupert, M. G. Vergniory, and S. S. Tsirkin, IrRep: Symmetry eigenvalues

and irreducible representations of *ab initio* band structures, Comput. Phys. Commun. **272**, 108226 (2022).

[75] L. Elcoro, B. Bradlyn, Z. Wang, M. G. Vergniory, J. Cano, C. Felser, B. A. Bernevig, D. Orobengoa, G. de la Flor, and M. I. Aroyo, Double crystallographic groups and their representations on the Bilbao Crystallographic Server, J. Appl. Crystallogr. **50**, 1457 (2017).

[76] J. M. Besson, E. H. Mokhtari, J. Gonzalez, and G. Weill, Electrical Properties of Semimetallic Silicon III and Semiconductive Silicon IV at Ambient Pressure, Phys. Rev. Lett. **59**, 473 (1987).

[77] C.-Y. Yeh, Z. W. Lu, S. Froyen, and A. Zunger, Zinc-blende-wurtzite polytypism in semiconductors, Phys. Rev. B **46**, 10086 (1992).

[78] T. B. Shiell, L. Zhu, B. A. Cook, J. E. Bradby, D. G. McCulloch, and T. A. Strobel, Bulk Crystalline 4*H*-Silicon through a Metastable Allotropic Transition, Phys. Rev. Lett. **126**, 215701 (2021).

[79] S. Pandolfi, C. Renero-Lecuna, Y. Le Godec, B. Baptiste, N. Menguy, M. Lazzeri, C. Gervais, K. Spektor, W. A. Crichton, and O. O. Kurakevych, Nature of hexagonal silicon forming via high-pressure synthesis: Nanostructured hexagonal 4H polytype, Nano Lett. **18**, 5989 (2018).

[80] O. Madelung and M. Schulz, *Numerical Data and Functional Relationships in Science and Technology, Crystal and Solid State Physics*, Landolt-Börnstein, New Series, Group III, Vol. 22 (Springer, Berlin, 1987).

[81] P. Käckell, B. Wenzien, and F. Bechstedt, Electronic properties of cubic and hexagonal SiC polytypes from *ab initio* calculations, Phys. Rev. B **50**, 10761 (1994).

[82] B. Farid and R. J. Needs, Energies of atoms and solids within the local-density approximation, Phys. Rev. B **45**, 1067 (1992).

[83] F. Bechstedt and A. Belabbes, Structure, energetics, and electronic states of III-V compound polytypes, J. Phys.: Condens. Matter **25**, 273201 (2013).

[84] J. von Boehm and P. Bak, Devil's Stairs and the Commensurate-Commensurate Transitions in CeSb, Phys. Rev. Lett. **42**, 122 (1979).

[85] C. Cheng, R. J. Needs, and V. Heine, Inter-layer interactions and the origin of SiC polytypes, J. Phys. C: Solid State Phys. **21**, 1049 (1988).

[86] S. Limpijumnong and W. R. L. Lambrecht, Total energy differences between SiC polytypes revisited, Phys. Rev. B **57**, 12017 (1998).

[87] L. F. Mattheiss and J. R. Patel, Electronic stacking-fault states in silicon, Phys. Rev. B **23**, 5384 (1981).

[88] M. Y. Chou, M. L. Cohen, and S. G. Louie, Theoretical study of stacking faults in silicon, Phys. Rev. B **32**, 7979 (1985).

[89] P. J. H. Denteneer, Stacking-fault energies in silicon, diamond, and silicon carbide, MRS Online Proc. Libr. **141**, 343 (1988).

[90] A. Gross and H. Teichler, Real-space method for total-energy calculations in semiconductors: Estimationx of stacking fault energies, Philos. Mag. B **64**, 413 (1991).

[91] P. Käckell, J. Furthmüller, and F. Bechstedt, Stacking faults in group-IV crystals: An *ab initio* study, Phys. Rev. B **58**, 1326 (1998).

[92] H. Föll and C. B. Carter, Direct TEM determination of intrinsic and extrinsic stacking fault energies of silicon, Philos. Mag. A **40**, 497 (1979).

[93] S. Takeuchi and K. Suzuki, Stacking fault energies of tetrahedrally coordinated crystals, Phys. Status Solidi A **171**, 99 (1999).

[94] J. H. Kim and J. Y. Lee, High-resolution transmission electron microscopy study of pulsed laser beam crystallized Si thin film: the formation of hexagonal Si and defects, Thin Solid Films **292**, 313 (1997).

[95] R. W. G. Wyckoff, *Crystal Structures* (Interscience, New York, 1964).

[96] C. Kittel, *Introduction to Solid State Physics* (Wiley, New York, 2005).

[97] S. Q. Wang and H. Q. Ye, *Ab initio* elastic constants for the lonsdaleite phases of C, Si and Ge, J. Phys.: Condens. Matter **15**, 5307 (2003).

[98] J.-M. Wagner and F. Bechstedt, Properties of strained wurtzite GaN and AlN: *Ab initio* studies, Phys. Rev. B **66**, 115202 (2002).

[99] Y. Wei, J. Li, X. Shi, J. Li, and C. He, First-principles study on the electronic, mechanical and optical properties for silicon allotropes in hexagonal 2–7 stacking orders, Scr. Mater. **219**, 114843 (2022)..

[100] P. Borlido (private communication) (2023).

[101] W. Martienssen and H. Warlimont, *Springer Handbook of Condensed Matter and Materials Data* (Springer, Berlin, 2005).

[102] Z.-L. Liu, C. E. Ekuma, W.-Q. Li, J.-Q. Yang, and X.-J. Li, ELASTOOL: An automated toolkit for elastic constants calculation, Comput. Phys. Commun. **270**, 108180 (2022).

[103] E. R. Fuller and W. F. Weston, Relation between elastic constant tensors of hexagonal and cubic structures, J. Appl. Phys. **45**, 3772 (1974).

[104] T. Liang, L. Xiong, H. Lou, F. Lan, J. Zhang, Y. Liu, D. Li, Q. Zeng, and Z. Zeng, Mechanical properties of hexagonal silicon, Scr. Mater. **220**, 114936 (2022).

[105] A. Schleife, F. Fuchs, C. Rödl, J. Furthmüller, and F. Bechstedt, Branch-point energies and band discontinuities of III-nitrides and III-/II-oxides from quasiparticle band-structure calculations, Appl. Phys. Lett. **94**, 012104 (2009).

[106] A. Belabbes, S. Botti, and F. Bechstedt, Band lineup at hexagonal $Si_xGe_{1-x}/Si_yGe_{1-y}$ alloy interfaces, Phys. Rev. B **106**, 085303 (2022).

[107] G. F. Koster, J. O. Dimmock, R. G. Wheeler, and H. Statz, *Properties of the Thirty-Two Point Groups* (MIT Press, Cambridge, MA, 1963).

[108] M. R. Salehpour and S. Satpathy, Comparison of electron bands of hexagonal and cubic diamond, Phys. Rev. B **41**, 3048 (1990).

[109] M. Murayama and T. Nakayama, Chemical trend of band offsets at wurtzite/zinc-blende heterocrystalline semiconductor interfaces, Phys. Rev. B **49**, 4710 (1994).

[110] P. Tronc, Y. Kitaev, G. Wang, M. Limonov, A. Panfilov, and G. Neu, Optical selection rules for hexagonal GaN, Phys. Status Solidi B **216**, 599 (1999).

[111] Y. E. Kitaev and P. Tronc, Exact symmetries of electron states and optical selection rules in wurtzite-based nanostructures, Phys. Rev. B **64**, 205312 (2001).

[112] A. Schleife, C. Rödl, F. Fuchs, J. Furthmüller, and F. Bechstedt, Strain influence on valence-band ordering and excitons in ZnO: An *ab initio* study, Appl. Phys. Lett. **91**, 241915 (2007).

[113] S. L. Chuang and C. S. Chang, k·p method for strained wurtzite semiconductors, Phys. Rev. B **54**, 2491 (1996).

[114] C. Fasolato, M. De Luca, D. Djomani, L. Vincent, C. Renard, G. Di Iorio, V. Paillard, M. Amato, R. Rurali, and I. Zardo, Crystalline, phononic, and electronic properties of heterostructured polytypic Ge nanowires by Raman spectroscopy, Nano Lett. **18**, 7075 (2018).

[115] P.-S. Chen, S.-T. Fan, H.-S. Lan, and C. W. Liu, Band calculation of lonsdaleite Ge, J. Phys. D: Appl. Phys. **50**, 015107 (2017).

[116] N. Zhang, J. Yan, L. Wang, J. Zhang, Z. Zhang, T. Miao, C. Zheng, Z. Jiang, H. Hu, and Z. Zhong, Unique hexagonal-Ge nanostructures with direct-bandgap emissions in Si-based light-emitting metasurface, Research Square, https://doi.org/10.21203/rs.3.rs-2037989/v1.

[117] F. Fabbri, E. Rotunno, L. Lazzarini, N. Fukata, and G. Salviati, Visible and infra-red light emission in boron-doped wurtzite silicon nanowires, Sci. Rep. **4**, 3603 (2014).

[118] M. Amato, T. Kaewmaraya, A. Zobelli, M. Palummo, and R. Rurali, Crystal phase effects in Si nanowire polytypes and their homojunctions, Nano Lett. **16**, 5694 (2016).